AUTHOR(S)
Ma, J., Hua, Y., Cao, Y., Jia, C., & Li, J.

TITLE
Anchoring $Cu_2O$ nanoparticles on g-$C_3N_4$ nanosheets for enhanced photocatalytic performance

YEAR
2024

DOI
10.1016/j.fuel.2024.131139

CITATION
Ma, J., Hua, Y., Cao, Y., Jia, C., & Li, J. (2024). Anchoring $Cu_2O$ nanoparticles on g-$C_3N_4$ nanosheets for enhanced photocatalytic performance. *Fuel, 364*, 131139. https://doi.org/10.1016/j.fuel.2024.131139

VERSION
Accepted Manuscript

# Anchoring $Cu_2O$ nanoparticles on g-$C_3N_4$ nanosheets for enhanced photocatalytic performance

Jian Ma[a,b*], Yingjie Hua[b], Yuanke Cao[b], Chunman Jia[a], Jianwei Li[a,c*]

[a] Hainan Provincial Key Laboratory of Fine Chem, School of Chemistry and Chemical Engineering, Hainan University, Haikou, 570228, P. R. China

[b]School of Chemistry and Chemical Engineering of Hainan Normal University, Key Laboratory of Electrochemical Energy Storage and Energy Conversion of Hainan Province, Haikou, 571158, P. R. China

[c] MediCity Research Laboratory, University of Turku, Tykistökatu 6, Turku 20520, Finland.

*Corresponding authors: Jian Ma, Jianwei Li, E-mail address: majian4552@126.com, jianwei.li@utu.fi

**Abstract**

Photocatalytic $H_2$ evolution technology has sparked intense attention as a potential solution to the energy problem and environmental pollution. $Cu_2O$ has emerged as a promising photocatalyst for $H_2$ production due to its narrow bandgap, suitable conduction band (CB) position, and easy synthesis. However, overcoming the disadvantage of photocorrosion, which limits the use of $Cu_2O$ in hydrogen production, remains a problem. In this work, g-$C_3N_4$ nanosheets were introduced as a support and hole acceptor for $Cu_2O$. Experimental results and density functional theory calculation confirmed the creation of heterojunctions at the interface between $Cu_2O$ and g-$C_3N_4$ nanosheets, which allows the transfer and separation of photogenerated carriers, resulting in an increased photocatalytic $H_2$ production rate (1796.8 μmol/g/h) and outstanding stability. In addition, the composite photocatalyst exhibits an enhanced tetracycline hydrochloride (TC) degradation activity. A “Z-scheme”

photocatalysis mechanism involved in the improvement of the composite photocatalyst's capacity was clearly illustrated. This study reveals that two-dimensional materials with rich functional groups can modify $Cu_2O$ for effective photocorrosion inhibition and enhanced photocatalytic activities.

**Keywords:** g-$C_3N_4$ nanosheets; $Cu_2O$; heterojunction; Photocatalytic hydrogen evolution; Photodegradation

## 1 Introduction

In recent years, the energy crises and environmental pollution have become a development burden[1-5]. The development and use of hydrogen energy are seen as one of the most promising paths to resolve the energy crisis[6,7]. Photocatalytic water splitting, which can generate hydrogen using renewable solar power, offers a wide range of applications[8-11]. The property of photocatalysts, which are held by semiconductors, plays a crucial role in the process. Transition metal oxides are often used to construct photocatalysts due to their easy preparation and morphology control. $Cu_2O$, as one of the transition metal oxides, is found to be an ideal candidate for the photocatalytic $H_2$ evolution due to its cheap, non-toxic, visible light response and negative CB position [12-14]. Unfortunately, single $Cu_2O$ has the disadvantages of instability and low photocatalytic activity, for the Cu (I) of $Cu_2O$ suffers readily from oxidation under light irradiation due to the photogenerated holes not compensated by electrons[15,16], leading to a so called photocorrosion. Interestingly, coupling $Cu_2O$ with another material, and constructing binary materials with heterostructure can effectively separate electron-hole pairs, resulting in high photocatalytic efficiency[17]. To date, various $Cu_2O$ based photocatalysts have been constructed to improve its $H_2$ evolution activity, such as $TiO_2/Cu_2O$[18], Zn-MOF/$Cu_2O$[19], $CdS/Cu_2O$[20], $Au@Cu_2O/Ta_3N_5$[21], $In(OH)_3$-$In_2S_3$-$Cu_2O$[22], $WO_3/Cu_2O$[23], g-$C_3N_4/Cu_2O$[24-26]

etc. Therein, g-$C_3N_4$ is a polymeric organic semiconductor with narrow band gap (~2.6 eV). It is not only inexpensive, but also stable in chemical property[27-30]. Specifically, the band gap energy level of g-$C_3N_4$ matches well with that of $Cu_2O$[31]. Among the g-$C_3N_4$/$Cu_2O$ composites, by designing a Z-scheme heterojunction can fully utilize the reducibility of photoinduced electrons of PS Ⅰ ($Cu_2O$). Meanwhile, the photogenerated holes can be neutralized by the photoelectrons from PS Ⅱ (g-$C_3N_4$), thus concomitantly restrain the photocorrosion of $Cu_2O$[32]. Recent study has shown that the band gap energy levels of g-$C_3N_4$ and $Cu_2O$ make it possible to form Z-scheme heterojunction when they are composited[33].

There are many ways to form the g-$C_3N_4$/$Cu_2O$ composite. Zhang et al[34] prepared a series of ultrafine $Cu_2O$ on the LDH support, and found that reducing the particle size of $Cu_2O$ is beneficial for improving the charge separation efficiency. Therefore, choosing appropriate support that can compensate photogenerated holes from $Cu_2O$ is a promising strategy for avoiding photocorrosion. As we know, the charge separation efficiency of bulk g-$C_3N_4$ is relatively low for the inherent surface defects and weak van der Waals force between layers[35]. The work of Niu et al [36] has showed that g-$C_3N_4$ nanosheets possess a large surface area, improved electron transport ability along the in-plane direction and prolonged lifetime of charge carriers. More importantly, the interface inside the composite material is the key to electron transport process[37]. g-$C_3N_4$ nanosheets have abundant –$NH_2$, which can coordinate with $Cu^{2+}$ ions (in the preparation process) and enhance the stability of the composites[38].

Herein, in order to construct $Cu_2O$/g-$C_3N_4$ nanosheets with close interfacial connections, $Cu_2O$ nanocrystals have been grown on g-$C_3N_4$ nanosheets via a series *in situ* adsorption, reduction and deposition processes in the present work. The particle size of $Cu_2O$ was controlled nanometer with the

action of surfactants. Subsequently, phase structure, morphology, band structure, and specific surface area of as-synthesized samples have been systematically characterized. The results of DFT calculations further identified the firmly combination between $Cu_2O$ and CN Ns. The content of $Cu_2O$ in the composite was optimized by photocatalytic $H_2$ evolution test. Furthermore, the photooxidation property of the optimal sample was evaluated by photodegradation of tetracycline hydrochloride (TC). The experimental results show that $Cu_2O$/g-$C_3N_4$ nanosheets composite presents excellent photocatalytic performance and meanwhile high stability. Furthermore, the separation and transfer process of photo-induced carriers was detailedly investigated to account for the photocatalysis mechanism. The photocorrosion of $Cu_2O$ is restrained due to the formation of Z-scheme heterojunction, which was especially confirmed by using KPFM technology.

## 2 Experimental

### 2.1 Preparation of photocatalysts

#### 2.1.1 Preparation of g-$C_3N_4$ nanosheets

A simple two-step calcination procedure was used to create the g-$C_3N_4$ nanosheets. First, 5 g of melamine was put into a crucible, which was then placed in a muffle furnace and heated at a rate of 2.5 ℃/min to 550 ℃ (in the air) and held there for 4 h. Pure g-$C_3N_4$ was achieved after cooling spontaneously to room temperature. The above g-$C_3N_4$ (0.4 g) powder was then cleaned in the air at 500 ℃ for 2 h (at a heating rate of 2 ℃/min) to produce g-$C_3N_4$ nanosheets. The g-$C_3N_4$ nanosheets were labeled as CN Ns.

#### 2.1.2 Preparation of $Cu_2O$/g-$C_3N_4$ nanosheets

To achieve a homogenous mixture, a given amount of as-prepared CN Ns was dispersed in 50 mL of deionized water and stirred for 30 min. The aforementioned combination was then dissolved with 60

mg of $Cu(AC)_2•H_2O$, 0.1 g CTAB and 0.1 g EDTA, respectively. The mixture was then mixed with 20 mL of ascorbic acid (0.3 mol/L) and 20 ml of NaOH (0.45 mol/L). After stirring for 30 min, the precipitate was separated by centrifugation and washed multiple times with deionized water and ethanol. The product was dried for 10 h in a vacuum at 60 °C to obtain the $Cu_2O/g\text{-}C_3N_4$ nanosheets. The mass ratios of $Cu_2O$ in the $Cu_2O/g\text{-}C_3N_4$ nanosheets were 10%, 20%, and 30%, respectively, and the corresponding samples were labeled as CCN-x (x is the weight ratio of $Cu_2O$ in the composite). In the same circumstance, pure $Cu_2O$ was prepared without the addition of CN Ns.

**2.2 Characterization of photocatalysts**

X-ray diffraction (XRD, Cu-Kα radiation source, 40 kV × 140 mA, Ultimalv type, Bruker, Germany) was used to examine the phase structure of the as-prepared samples. The contents of C, N elements in $g\text{-}C_3N_4$ and CN Ns samples were determined using elemental analysis (Flash EA 1112, Thermo Finnigan). The FT-IR spectra of the samples were recorded on a Nicolet 6700 infrared spectrometer (Thermo scientific, USA) using KBr pellet. The sample morphologies were examined using a scanning electron microscope (SEM, Hitachi S-4800, Japan) and a transmission electron microscope (TEM, Tecnai G2 F20, USA). Atomic force microcopy (AFM) images were recorded by scanning probe microscope (NT-MDT NTEGRA, Russia). The surface elemental compositions of samples were analyzed by X-ray photoelectron spectroscopy (XPS, K-alpha, Thermo, Germany). UV-vis diffuse reflectance spectra of samples were determined using a UV-vis spectrophotometer (T10, Beijing General Instrument Co., Ltd., China). The wavelength ranged from 200 to 800 nm. An $N_2$ adsorption/desorption equipment apparatus was used to measure the specific surface area and total pore volume of samples (BET, Kubo X1000, China). A fluorescence spectrometer (Horiba, Fluorolog-3, USA) was used to acquire photoluminescence (PL) spectra of samples. The in situ electron spin

resonance (ESR) measurements were carried out on an ESR spectrometer (100 kHz, 1.0 mV, JES-FA200, JEOL, Japan), with DMPO in water solution, and a 500 W high-pressure mercury lamp equipped with a cutoff filter ($\lambda \geq 420$ nm) was used as illumination source. Liquid chromatography-mass spectrometry (LC-MS, Thermofisher U3000-Q Exactive Focus, USA) was used to analyze the possible intermediates produced during TC degradation. Surface potential distribution of CCN-20 under dark and $\lambda > 400$ nm conditions were measured by the Kelvin probe force microscopy (KPFM) at scanning probe microscope (SPM) system (Bruker Dimension icon, Germany).

**2.3 Photocatalytic evaluation**

The photocatalytic hydrogen evolution rate of the samples was investigated in a close gas circulation system. A 300 W Xenon lamp ($\lambda \geq 420$ nm, HSX-F300, Beijing NBet Technology Co., Ltd.) was employed as light source. The intensity of light was 100 mW/cm$^2$. Firstly, 100 mg photocatalyst was dispersed in 100 ml deionized water, followed by 10 ml triethanolamine (sacrificial reagent) and 133 μL chloroplatinic acid ($H_2PtCl_6$, 0.5 wt% Pt, cocatalyst) added under magnetic stirring to the aforesaid suspension. After the loading of the cocatalyst and vacuuming, $H_2$ evolution over the sample was carried out. The produced $H_2$ was analyzed by gas chromatography (GC-2014, Shimadzu, Japan).

The apparent quantum yield (AQY) was measured and calculated according to AQY (%) = [2 × N($H_2$) / N(photon)] × 100%, where N($H_2$) and N(photon) represent the evolved amount of $H_2$ and the number of incident photons, respectively.

In addition, photodegradation of TC was carried out to evaluate the photooxidation properties of the CCN-20 sample. In each test, 50 mL of TC aqueous solution (20 mg/L) was placed in a quartz bottle, and 20 mg of catalyst was dispersed in the solution. Then, the mixture was kept in dark under

continuous stirring for 0.5 h until it got to adsorption-desorption equilibrium. After that, a 300 W Xenon lamp (HSX-F300, NBet, China) equipped with a cutoff filter ($\lambda \geq 420$ nm) was adopted as the illumination source for photocatalytic experiments. The light intensity was 100 mW/cm$^2$. The concentration variation of TC solution was determined using a UV–vis spectrophotometer (T10 type, General analysis, China). The scavenging experiments in the photodegration process were carried out by the addition of isopropanol (IPA, ·OH scavenger, 2 mL), benzoquinone (pBQ, $\cdot O_2^-$ scavenger, 1.25 mg), or EDTA-2Na (hole scavenger, 1.25 mg), respectively.

**2.4 Photoelectrochemical measurements**

An electrochemical system (CHI 660, Chenhua, Shanghai, China) was used to conduct a photoelectrochemical (PEC) experiment. The electrochemical system was outfitted with a three-electrode configuration electrode (the sample was deposited on an FTO as a photoanode; a Pt wire was utilized as a counter electrode, and a saturated calomel electrode was employed as a reference electrode). A 0.1 M $Na_2SO_4$ solution was used as the supporting electrolyte. A 300 W Xenon lamp ($\lambda \geq$ 420 nm, HSX-F300, Beijing NBet Technology Co., Ltd.) was used as a light source. In the electrochemical impedance spectroscopy (EIS) measurement, the frequency of alternating current (AC) was 100 kHz–0.1 Hz. Before starting the photoelectrochemical process, the reaction system was purged with high-purity $N_2$ for 30 min to dissolve oxygen.

**2.5 Calculation details**

All calculations were carried out with Vienna Ab-initio Simulation Package(VASP)[39] with the projector augmented wave (PAW) method[40]. The exchange-functional was treated using the Perdew-Burke-Ernzerhof (PBE)[41] functional in combination with the DFT-D3 correction[42], to describe the weak interactions between atoms. The cut-off energy of the plane-wave basis was set at

450 eV in structural optimization. For the optimization of both geometry and lattice size, the Brillouin zone integration was performed with a Monkhorst-Pack *k*-point mesh of 0.03 $Å^{-1}$. Partial occupancies of the Kohn−Sham orbitals were allowed using the Gaussian smearing method and a width of 0.05 eV. A geometry optimization was considered convergent when the energy change was smaller than 0.02 eV $Å^{-1}$. The vacuum spacing in a direction perpendicular to the plane of the structure is 15 Å. Spin polarization was included for the correct description of magnetic properties. To consider the strong correlation effects of transition metal in structure, both structural optimizations and electronic structure calculations were carried out by using the spin-dependent GGA plus Hubbard correction U method, and the effective $U_{eff}$ parameter is 4.0 eV for Cu atom.

## 3 Results and discussion

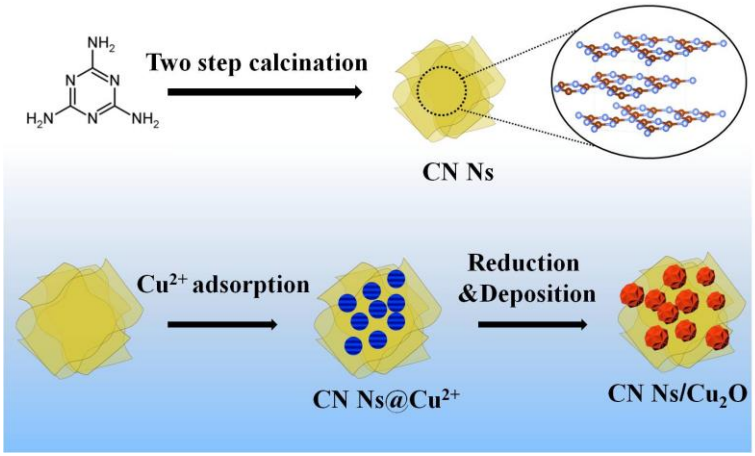


Scheme 1. Schematic diagram of the preparation process for CCN-x.

As depicted in Scheme 1, CN Ns was easily obtained by etching bulk g-$C_3N_4$ using thermal oxidation. Due to the damage of weak van der Waals interactions between CN layers, CN Ns have improved physicochemical properties as compared to bulk g-$C_3N_4$. One of the most important features is that more amino (–$NH_2$) and hydroxyl (–OH) groups can be exposed in the structure of CN Ns. The existence of lone pair electrons in –$NH_2$ and hydroxyl –OH can form an electron-rich

microenvironment[43], which is beneficial to coordinate with $Cu^{2+}$ ions and form CN Ns@$Cu^{2+}$. Under the influence of ascorbic acid reduction, accompanied by the introduction of NaOH, CN Ns@$Cu^{2+}$ gradually transforms into CN Ns/$Cu_2O$[44]. In addition, the particle size of $Cu_2O$ was controlled nanometer with the action of surfactants(see in the morphology analysis section).

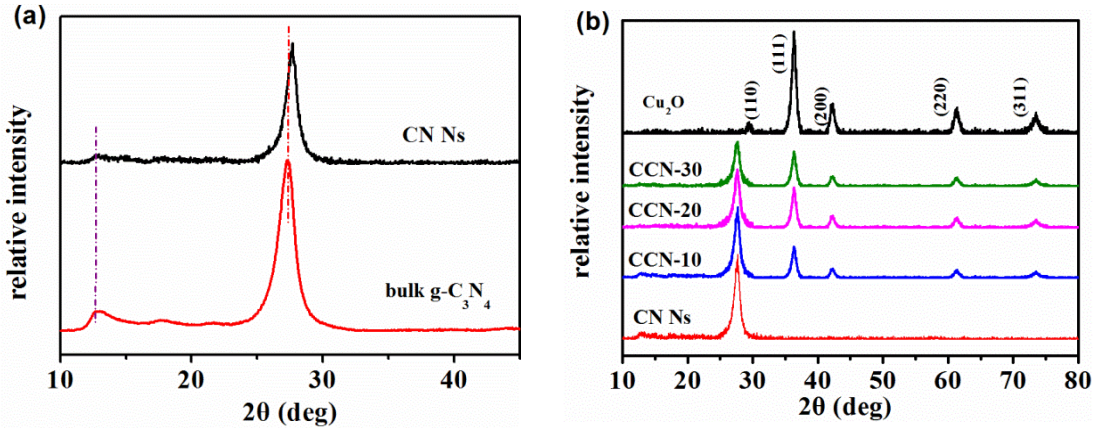


Fig. 1 XRD patterns of as-prepared samples.

X-ray diffraction (XRD) was used to characterize the phase structure of the as-prepared samples. As shown in Fig. 1a, the XRD pattern of bulk g-$C_3N_4$ shows two diffraction peaks. The low-angle reflection peak at 13.1° corresponds to the lattice planes parallel to the *c*-axis, whereas the major peak at 27.3° results from the interplanar stacking of aromatic systems[45]. The diffraction peaks of CN Ns are consistent with bulk g-$C_3N_4$, indicating that the major crystal structure of g-$C_3N_4$ is maintained in the nanosheets. A closer look reveals that the peak at 27.3° in the CN Ns shifts toward the high angle while the intensity of diffraction peaks weakens, suggesting a decrease in the distance between layers. This could be due to two reasons: first, the CN layers were planarized in the bulk g-$C_3N_4$ heating process, shortening the interplanar gap of the laminar g-$C_3N_4$. Second, as can be seen from the elemental analysis results (Table S1), some carbon atoms were lost in the bulk g-$C_3N_4$ heating process, thus decreased the distance between CN layers[46]. As shown in Fig. 1b, all the diffraction peaks of $Cu_2O$ at 29.4°, 36.5°, 42.2°, 61.2°, and 73.5° correspond to the diffraction of the (110), (111), (200),

(220), and (311) planes of cubic $Cu_2O$ (JCPDS NO. 05-0667) [47]. All the characteristic diffraction peaks of g-$C_3N_4$ and $Cu_2O$ may be seen in CCN-x composite sample. There are no apparent differences in the location of diffraction peaks when compared to pure CN Ns, showing that the addition of $Cu_2O$ has not affected the crystal structure of CN Ns. It can be observed that the strength of diffraction peaks corresponding to CN Ns in CCN-x composite samples progressively diminishes as the $Cu_2O$ concentration increases, which resulted from the coverage of $Cu_2O$ on the surface of CN Ns.

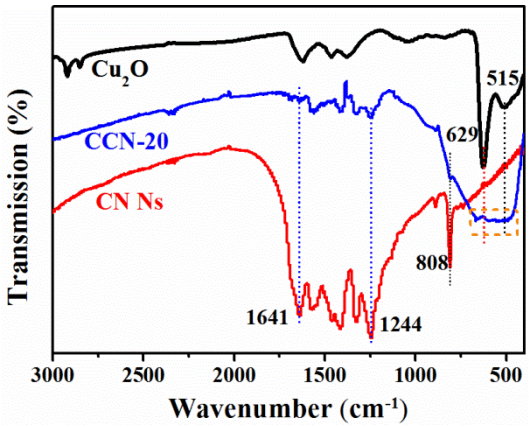


Fig. 2 FT-IR spectra of CN Ns, $Cu_2O$ and CCN-20 samples.

The chemical structures of the as prepared samples were further characterized by FT-IR. As shown in Fig. 2, CN Ns presents a peak at 808 $cm^{-1}$ of the out of plane bending mode of heptazine rings. The peaks between 1244 and 1641 $cm^{-1}$ were ascribed to the stretching modes of aromatic C-N heterocycles[48]. For pure $Cu_2O$, the absorption peaks at 515 $cm^{-1}$ and 629 $cm^{-1}$ are derived from the Cu-O vibration [49]. Both the characteristic peaks of CN Ns and the vibration peak of $Cu_2O$ are all observed in CCN-20 sample, confirming that $Cu_2O$ was successfully combined with CN Ns, being consistent with the XRD result mentioned above. It is worth noting that the intensity of the absorption peaks corresponding to aromatic C-N heterocycles was obviously decreased compared to those in CN Ns. According to previous reports[50], it can be deduced that N atoms were partially coordinated with Cu atoms, thus reduced the vibration of aromatic C-N heterocycles.

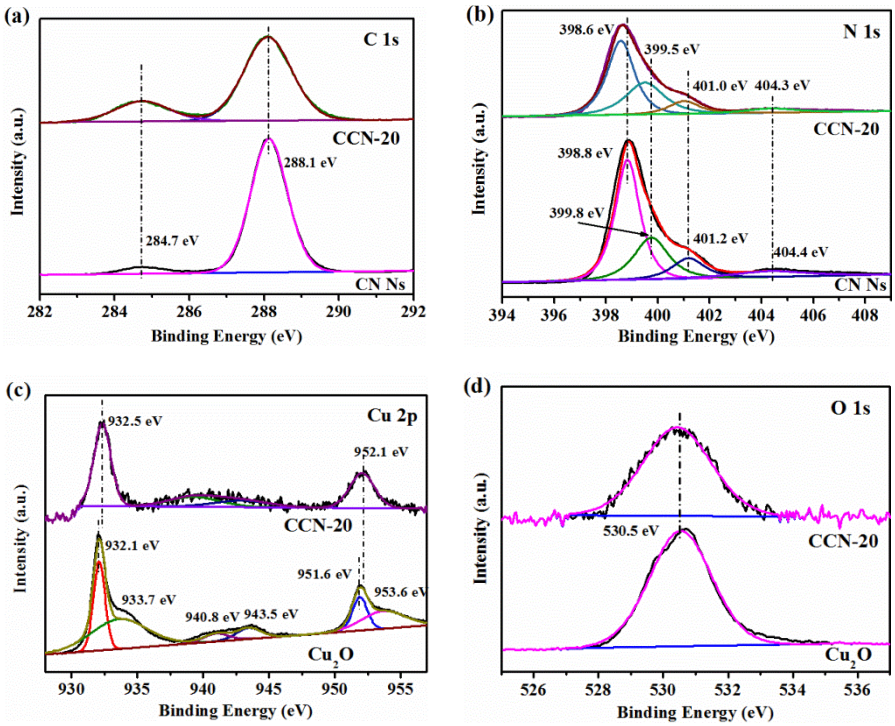


Fig. 3 The XPS spectra of (a) C 1s, (b) N 1s, (c) Cu 2p, and (d) O 1s of the samples.

The chemical state of the CN Ns, $Cu_2O$ and CCN-20 samples were determined using X-ray photoelectron spectroscopy (XPS) measurements. As shown in Fig. 3a, the C 1s spectra of CN Ns and CCN-20 with the two peaks at 284.7 eV and 288.1 eV are assigned to the surface adventitious carbon species and N-C=N groups, respectively[51]. The N 1s spectra of CN Ns and CCN-20 (Fig. 3b) can be fitted into four peaks at binding energies of ~398, ~399, ~401 and ~404 eV, corresponding to triazine ring $sp^2$ hybridization C=N-C, N-$C_3$, C-N-H and π excitations, respectively[52]. As to $Cu_2O$ and CCN-20 samples, the two peaks of Cu 2p spectra (Fig. 3c) located at ~932 eV and ~951 eV can be ascribed to the characteristic Cu $2p_{3/2}$ and Cu $2p_{1/2}$ peaks of $Cu^+$, respectively[17]. The additional peaks at ~933, ~940, and ~943 eV were assigned to the higher valence state of Cu, indicating that a small amount of $Cu^+$ can be oxidized under natural light irradiation[53] (the state of Cu will be discussed below). It was notable that compared with those in CN Ns, the binding energies of N 1s spectra in CCN-20 shifted lower to some extent (0.3~ 0.1eV), implying an increase in electron density. Whereas

the peak positions of Cu $2p_{3/2}$ and Cu $2p_{1/2}$ in CCN-20 shift ~0.5 eV to the direction of higher binding energy, confirming a reduction in electron density[54]. According to these phenomena and previous reports[55,56], it can be deduced that strong interaction existing between Cu and N atoms in the CCN-20 composite. This is in accordance with the above FT-IR results. Moreover, these observations would clarify some electron migrations from $Cu_2O$ to CN Ns under darkness. Since the Fermi level of electrons in $Cu_2O$ is higher than that in CN Ns, when these two semiconductors come into contact in dark, meeting the thermodynamic requirement of Fermi level equilibrium makes electrons transfer from $Cu_2O$ to CN Ns[57]. The peaks at 530.5 eV in the O 1s spectra (Fig. 3d) are attributed to the lattice oxygen in $Cu_2O$ and CCN-20 [47]. Since the XPS results can be influenced by the chosen test area, the peak intensities corresponding to Cu and O are relatively weak.

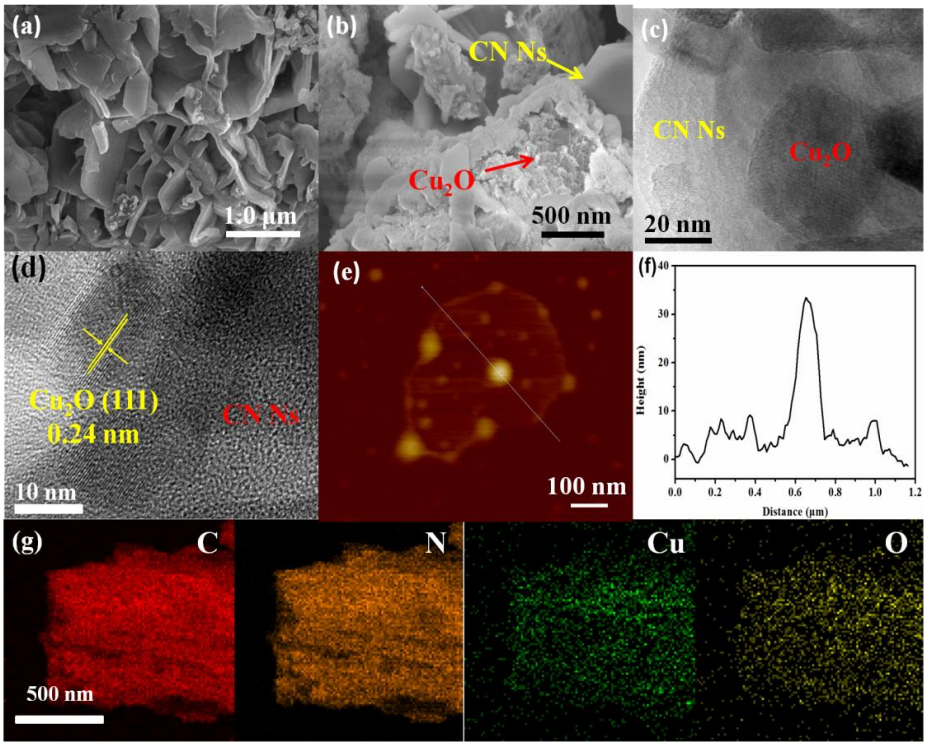


Fig. 4 SEM images of (a) CN Ns, (b) CCN-20. (c), (d) TEM images of CCN-20. (e) AFM image of CCN-20, and (f) the corresponding height profile of CCN-20. (g) elemental distribution of CCN-20 sample.

To elucidate the morphology of the produced samples, g-$C_3N_4$, CN Ns, $Cu_2O$, and CCN-20 were measured by SEM. As shown in Fig. S1a, pristine g-$C_3N_4$ has a block shape with varying sizes. The morphology of CN Ns is a thin flake form with uneven length and width of a nanoscale thickness (Fig. 4a). The $Cu_2O$ sample has a considerable number of particles, the size of which is around 50–60 nm, as illustrated in Fig. S1b. It can be seen from Fig. 4b that a large number of $Cu_2O$ nanoparticles are deposited on the surface of the CN Ns. In order to get the data concerning the specific surface area of bulk g-$C_3N_4$, CN Ns and CCN-20 samples, their $N_2$ adsorption–desorption isotherms were measured, and the results are shown in Fig. S2. It can be seen that the $N_2$ adsorption–desorption isotherms of the samples present type IV with hysteresis loop, confirming the existence of mesopores, which was formed between primary crystallites[58]. Based on the results, the specific surface areas of bulk g-$C_3N_4$, CN Ns, and CCN-20 were estimated to be 17.83 $m^2/g$, 66.5 $m^2/g$, and 29.4 $m^2/g$, respectively. This change is due to the morphology of the samples. Compared with bulk g-$C_3N_4$, CN Ns show a much larger surface area, which is due to the damage to the layered structure. This result also supports our previous assertion. Furthermore, the surface area of CN Ns was reduced with the introduction of $Cu_2O$, indicating that the surface of CN Ns was partially occupied by $Cu_2O$ nanoparticles. TEM was conducted to get more information about the interior structure of CCN-20 sample. Fig. 4c reveals the farctate structure inside the composite material. The appearance of CN Ns in the CCN-20 sample is quite similar to that of graphene[59]. In the case of high resolution, the crystal face of $Cu_2O$ nanoparticles in the CCN-20 composite could clearly be observed (Fig. 4d). Those major crystal faces with a spacing of 0.24 nm correspond to the (111) plane of cubic $Cu_2O$[26]. This is in accordance with the XRD results. Furthermore, the interface between CN Ns and $Cu_2O$ is naturally connected, which is beneficial to the charge transfer between the two semiconductors. Atomic force microscopy (AFM)

(Fig. 4e-f) reveals that some of the $Cu_2O$ nanoparticles on the surface of CN Ns were agglomerated, and the thickness of $Cu_2O$ is about 34 nm. The EDS mapping images from TEM (Fig. 4g) indicates the elemental distribution of CCN-20 with C, N, Cu and O, confirming that $Cu_2O$ was homogeneously deposited on CN Ns.

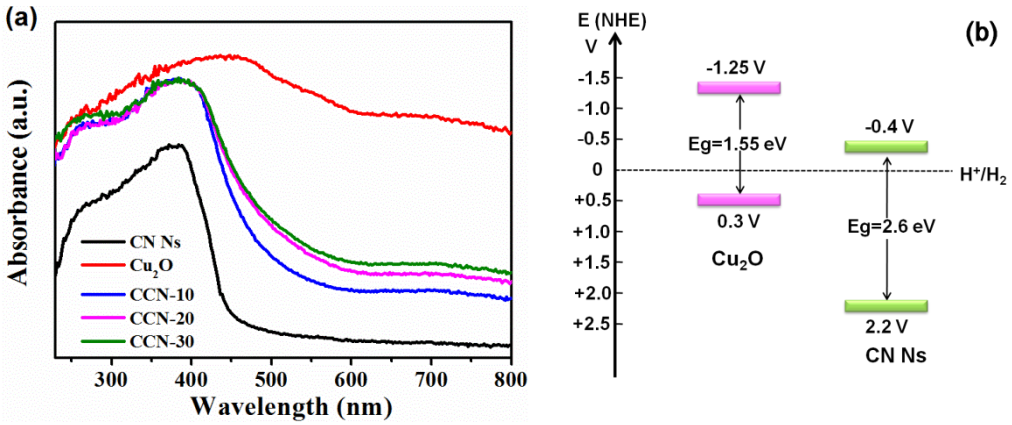


Fig. 5 (a) The UV-vis absorption spectra of the as-prepared samples. (b) The schematic illustration of the band structure of CN Ns and $Cu_2O$.

The photocatalyst's optical absorption property is critical to its activity. So, the solid UV-visible diffuse reflection absorption spectra of the prepared samples were recorded to examine their photoabsorption property. As presented in Fig. 5a, the absorption edge of pure CN Ns is around 450 nm, which resulted from the charge transfer from HOMO created by N 2p orbit to LUMO formed by C 2p orbit[60]. While the optical absorption property of $Cu_2O$ is strong in both UV and visible light regions, and its absorption peak is at about 475 nm. This can be ascribed to the small particle size of $Cu_2O$. The absorption margin of CCN-x samples lies between CN Ns and $Cu_2O$, both the extent of the absorption edge red shift and the visible light absorption intensity increase with increasing the $Cu_2O$ content are observed indeed, suggesting that the CCN-x composites can absorb more visible light than the pure CN Ns, which is crucial for enhancement of the photocatalytic reaction rate. The findings are related to the synergy of optical response of CN Ns and $Cu_2O$. Moreover, based on the above results and the Tauc

equation, the calculated bandgap energies of CN Ns and $Cu_2O$ are 2.6 eV and 1.55 eV, respectively (shown in Fig. S3).

XPS valance band spectra were used to determine the top position of VB in the potential coordinate system (vs.NHE) for the CN Ns and $Cu_2O$ samples. As shown in Fig. S4, the top potential of VB corresponding to CN Ns and $Cu_2O$ is estimated to be 2.2 and 0.3 V, respectively, in terms of intercepts. Hence, based on the VB potential and $E_g$ values of the samples, the CB bottom potentials for CN Ns and $Cu_2O$ can be predicted to be −0.4 V and −1.25 V, respectively. According to the above results, a schematic illustration of the band structures of the synthesized CN Ns and $Cu_2O$ can be drawn (as shown in Fig. 5b). It can be seen that the CB edge of CN Ns lies between the CB and VB potentials of $Cu_2O$. This implies that a "Z-scheme" electron transfer from the CB of CN Ns to the VB of $Cu_2O$ will take place when the composite is irradiated by visible light, which is important for facilitating the separation of photo-generated carriers and improving the redox capacity of photocatalyst (the mechanism will be discussed below).

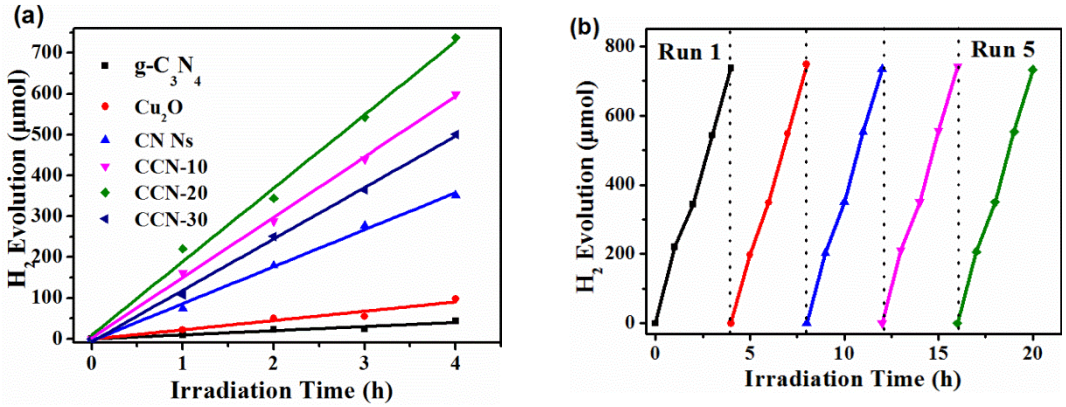

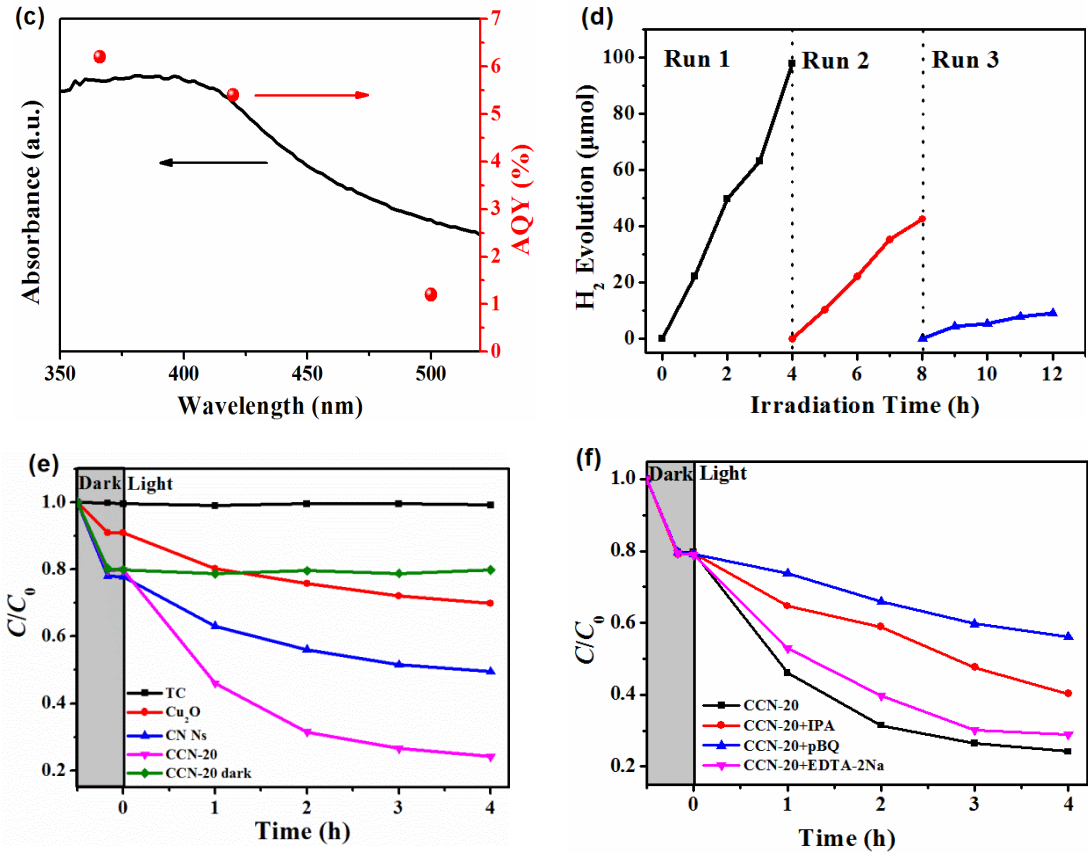


Fig. 6 (a) Photocatalytic activities for $H_2$ evolution of as-prepared samples under visible light irradiation. (b) Stability test of photocatalytic $H_2$ production activity over the CCN-20. (c) Wavelength dependence of the AQY of CCN-20. (d) Stability test of photocatalytic $H_2$ production activity over $Cu_2O$. (e) Photocatalytic activity of TC in the presence of CN Ns, $Cu_2O$, and CCN-20 under visible light irradiation. (f) Trapping tests of the photo-generated radicals in the photocatalytic degradation of TC.

To validate the distinct of the CCN-x composite materials' design strategy on photocatalytic $H_2$ evolution, the catalytic efficiency of pristine g-$C_3N_4$, CN Ns, $Cu_2O$, and CCN-x were assessed. The main function of Pt cocatalysts is to conduct the electrons out to the surface, thus facilitates proton reduction reaction[61]. As shown in Fig. 6a, the production of $H_2$ gradually increased as time went on. Pristine g-$C_3N_4$ presented little activity, while the CN Ns showed an enhanced $H_2$ evolution rate (905.7 μmol/g/h). The reason for this is that CN Ns have more active sites on the surface and higher charge

298 transfer efficiency than pure g-$C_3N_4$. The $H_2$ evolution rate of pure $Cu_2O$ (227.9 μmol/g/h) is also
299 relatively low, which can be ascribed to the self-oxidization of $Cu^+$ to $Cu^{2+}$. CCN-20 exhibits the most
300 prominent performance (1796.8 μmol/g/h) among these samples, which was found to be approximately
301 twice higher than that of pure CN Ns (approximately eight times higher than that of pristine $Cu_2O$).
302 This is because composite of CN Ns with $Cu_2O$ leads to a suitable energy level matching between CN
303 Ns and $Cu_2O$, which is more favorable to the photoelectron-hole transfer and separation compared to
304 the separate component, thus decreasing the recombination of electrons and holes. To compare the
305 photocatalytic activity of CCN-20, the photocatalytic hydrogen evolution rate of g-$C_3N_4$ and $Cu_2O$
306 based photocatalysts in recent years was listed (Table S2). As the content of $Cu_2O$ is more or less than
307 20%, the photocatalytic activity of CCN-x composite samples is decreased, demonstrating that 80% of
308 CN Ns needs 20% of $Cu_2O$ to form the optimum matching in material structure. Insufficiency or excess
309 of the $Cu_2O$ in content is all unfavorable to the photo-generated carriers' transfer and separation. The
310 stability of the CCN-20 sample was assessed by a recycling experiment of the $H_2$ evolution process.
311 Fig. 6b shows that the photocatalytic $H_2$ production activity of CCN-20 shows no obvious attenuation
312 after 5 cycles in 20 h. XRD, SEM and TEM of CCN-20 after the $H_2$ evolution experiment were carried
313 out to study the change in structure or morphology of this sample. As shown in Fig. S5, there are no
314 obvious changes in the crystal structure and morphology of the CCN-20 sample. Additionally, it can be
315 seen from Fig. S6a that the characteristic XPS peaks corresponding to $Cu^+$ ($2p_{3/2}$ at 932.5 eV and $2p_{1/2}$
316 at 952.2 eV) have no evident change in the Cu 2p spectrum of CCN-20 after the photocatalytic reaction.
317 These results indicate that CCN-20 sample is structurally robust and photocatalytically stable. The
318 apparent quantum yield (AQY) of CCN-20 sample was measured and calculated in order to more
319 accurately identify its photocatalytic $H_2$ production activity. As shown in Fig. 6c, it has achieved an

AQY of 5.4% at about 420 nm, and the variation tendency of AQY is generally correspond to its optical absorption spectrum. It also suggests that the $H_2$ production is primarily driven by photoinduced electrons in the composite material.

For comparison, the $H_2$ production stability of pure $Cu_2O$ was also evaluated, and the results are shown in Fig. 6d. It can be seen that the $H_2$ production activity of $Cu_2O$ decreased after 2 cycles. As shown in Fig. S6b, the positions of characteristic peaks of $Cu^+$( 932.1 eV and 951.8 eV) shifted to the high binding energy sides after the photocatalytic reaction. Meanwhile, the peaks at 933.6 eV, 940.9 eV, 943.4 eV and 953.7 eV were obviously increased. In order to study the role of the oxidized $Cu^+$, the Cu 2p XPS spectra of commercial CuO was measured, and the results are shown in Fig. S6c. From the comparison, it can be deduced that $Cu^+$ were partially oxidized to $Cu^{2+}$ after $H_2$ evolution experiment. This result implies that pure $Cu_2O$ is not stable in the photocatalytic process, which is attributed to its low carrier separation efficiency. As a result $Cu^+$ is readily oxidized by the photogenerated holes[62]. The above experimental results indicated that photocorrosion of $Cu_2O$ in CCN-20 can be effectively suppressed. In addition, it is necessary to investigate the effect of $Cu^{2+}$ on the photocatalytic activity since the presence of $Cu^{2+}$ in the sample before the photocatalytic reaction. Therefore, the photocatalytic $H_2$ evolution performance of CuO was tested in the same condition. As shown in Fig. S6d, CuO showed little $H_2$ production under visible light irradiation, indicating that tiny amount of $Cu^{2+}$ had no effect on photocatalytic $H_2$ evolution activity.

Photodegradation of TC was carried out to evaluate the photooxidation activity of CCN-20 sample, and the results are shown in Fig. 6e. It was indicated that CCN-20 also showed higher photocatalytic activity than those of pure CNNs and $Cu_2O$. After 4 h of visible light irradiation, the TC degradation efficiency for CCN-20 reached 76%. Additionally, blank tests confirm the role of light and catalysts in

TC degradation process. The in situ ESR measurements of CCN-20 were carried out in order to investigate the possible photooxidation mechanism. As shown in Fig. S7, signals corresponding to $\cdot O_2^-$ and ·OH radicals can all be detected after the CCN-20 had been irradiated for 10 min. Meanwhile, no signals were detected in dark. However, according to the band structures of CN Ns and $Cu_2O$ (Fig. 5b), the photoinduced holes of CNNs cannot oxidize surface hydroxyl species to form ·OH radicals ($E_0$(·OH/$OH^-$) = 2.4 V). On the other hand, the photoinduced electrons of $Cu_2O$ can easily combine with $O_2$ to form $\cdot O_2^-$ ($E_0$($\cdot O_2^-/O_2$) = -0.33 V) [63]. Hence, the formation process of ·OH can be deduced as follows:

$$\cdot O_2^- + e^- + H^+ \rightarrow \cdot OOH \quad (1)$$

$$\cdot OOH + H^+ \rightarrow H_2O_2 \quad (2)$$

$$H_2O_2 + e^- \rightarrow \cdot OH + OH^- \quad (3)$$

This indicate that both $\cdot O_2^-$ and ·OH really worked in the photodegradation process of TC. In order to verify the above deduce, scavenging experiments were carried out. Upon addition of scavengers of $\cdot O_2^-$, holes and ·OH radicals, respectively, such as pBQ, EDTA-2Na, and IPA into the reaction system, the rate of TC degradation slows down, especially in the case of adding pBQ and IPA (Fig. 6f). These results indicate again that the active species leading to TC degradation are mainly the $\cdot O_2^-$ and ·OH radicals generated by the photocatalytic process, being in accordance with the results of ESR detection.

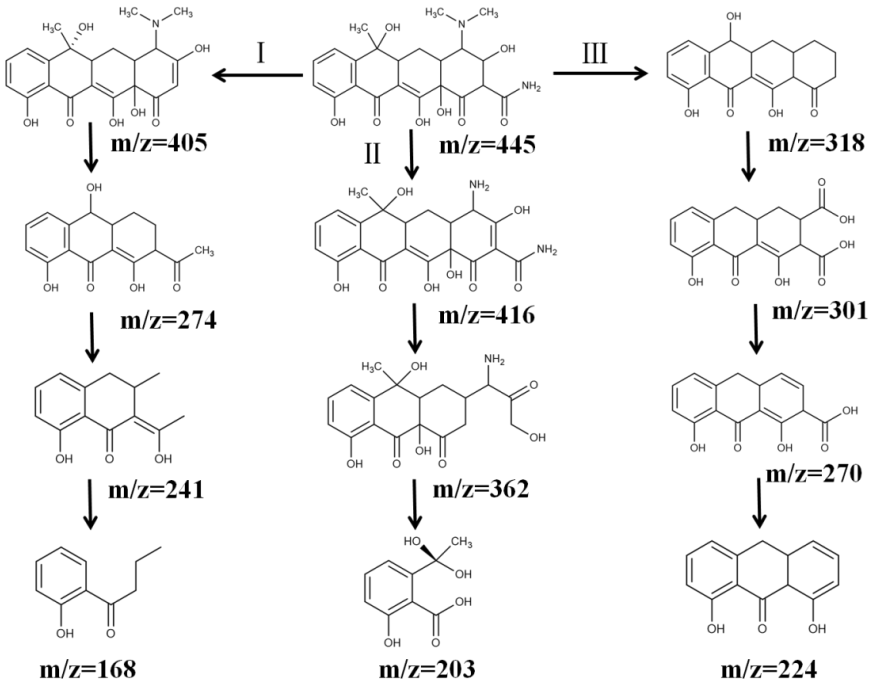


Fig. 7 Schematic representation of the possible degradation pathways and products during photocatalytic degradation of TC.

To get more information of the pathway for the TC degradation process by CCN-20, LC-MS was carried out to analyze the possible intermediates. The MS characteristic signal of the product is depicted in Fig. S8. It can be seen that TC molecules are progressively transformed into intermediates with smaller relative molecular weights. Based on the results, a possible reaction pathway of TC degradation can be deduced. As shown in Fig. 7, the intermediates undergo successive transformations ultimately resulting in some small molecular compounds, which can be mineralized. Therefore, it was implied that CCN-20 also has strong photooxidation ability.

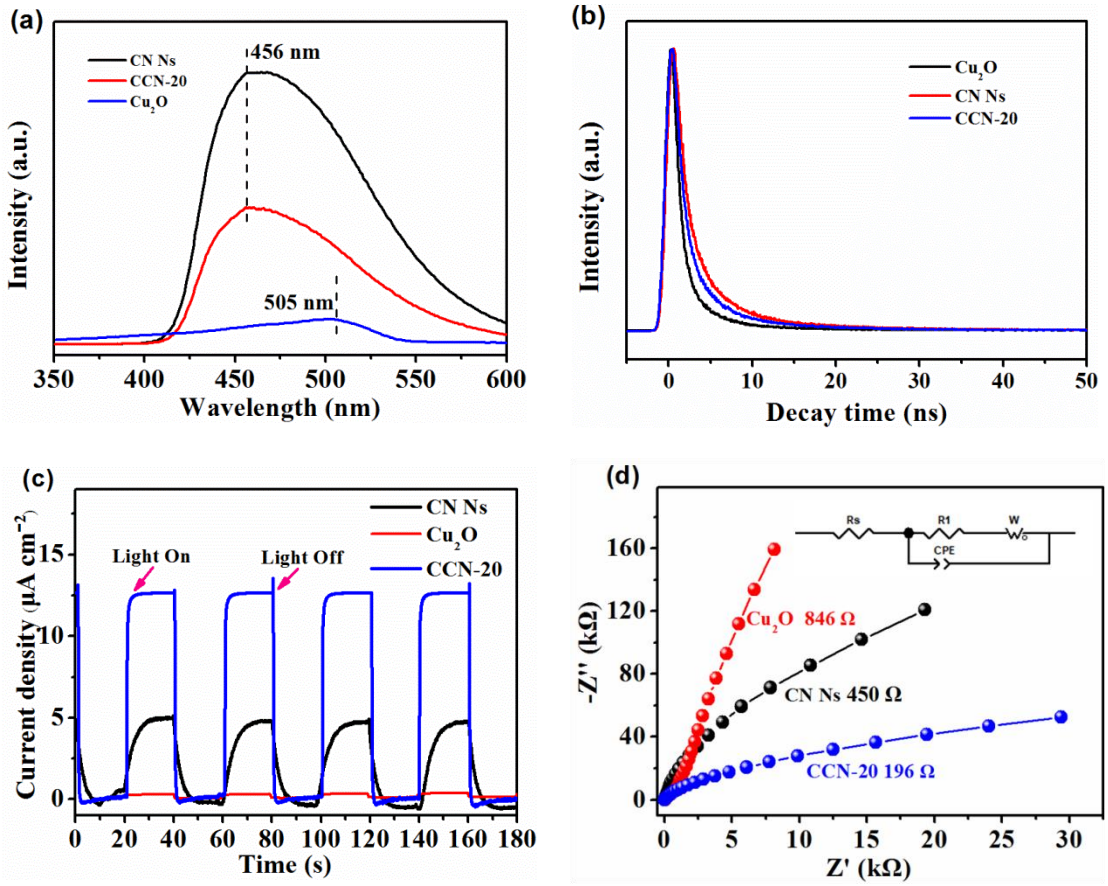


Fig. 8 (a) PL spectra of $Cu_2O$, CN Ns, and CCN-20. (b) Time-resolved PL spectra of $Cu_2O$, CN Ns, and CCN-20. (c) Transient photocurrent response of $Cu_2O$, CN Ns, and CCN-20. (d) EIS analysis of $Cu_2O$, CN Ns, and CCN-20.

The steady state fluorescence spectra of the CN Ns, $Cu_2O$ and CCN-20 samples (excited by 330 nm light) were recorded to investigate the separation behavior of photogenerated charge carriers. As shown in Fig. 8a, CN Ns exhibit an emission peak centered at about 456 nm. The emission peak is caused by n-π* electronic transitions in g-$C_3N_4$[64]. $Cu_2O$ presented the lowest intensity for the PL spectrum with an emission peak centered at about 505 nm, which can be ascribed to the emission of bandgap transition[57]. The introduction of $Cu_2O$ into CN Ns restrained the recombination of photogenerated electron-hole pairs in CN Ns, thus leading to a decrease in the PL emission intensity at 456 nm of CCN-20. Time-resolved PL spectra were utilized to see the charge transfer kinetics of the

materials. The results are shown in Fig. 8b, and the corresponding parameters are listed in Table S3(*A* is the pre-exponential factor)[57]. It can be seen that the PL average lifetime of CCN-20 (25.25 ns) was decreased in comparison with the CN Ns sample (29.21 ns), indicating the acceleration of charge transfer dynamics at the interfaces of the heterojunctions. The decrease of PL intensity and decay time of CCN-20 sample can be attributed to the well matched band structure of $Cu_2O$ and CN Ns, thus promotes the separation of photo-generated carriers.

To get more information about the separation of photogenerated electrons and holes, the transient photocurrent responses of CN Ns, CCN-20, and $Cu_2O$ were measured. As shown in Fig.8c, CCN-20 with higher photocatalytic activity demonstrated higher photocurrent intensity when compared to $Cu_2O$ and CN Ns. The charge carrier densities of, CN Ns, $Cu_2O$ and CCN-20 were estimated to be 4.9, 0.3 and 12.5 $\mu A/cm^2$. When $Cu_2O$ nanoparticles were deposited on the surface of CN Ns, the absorption capacity for visible light was increased (compared to CN Ns), and charge transport between the two semiconductors improved the separation efficiency of photogenerated charge carriers. Even so, the resistance of carrier migration also affects the separation efficiency of electron-hole pair. Thus, EIS measurements were performed to investigate the resistance of charge transfer in the materials, and the results are shown in Fig. 8d. It can be seen that CCN-20 has a smaller arc radius of EIS, indicating that the charge transfer resistance in the semiconductor-electrolyte interface was reduced in this sample. The equivalent circuit of the Nyquist diagram was fitted and the resistance values were derived. The resistance values of $Cu_2O$, CN Ns, and CCN-20 are 846, 450 and 196 Ω, respectively. These results align with the PL data, indicating improved separation efficiency of carriers in the CCN-20 sample.

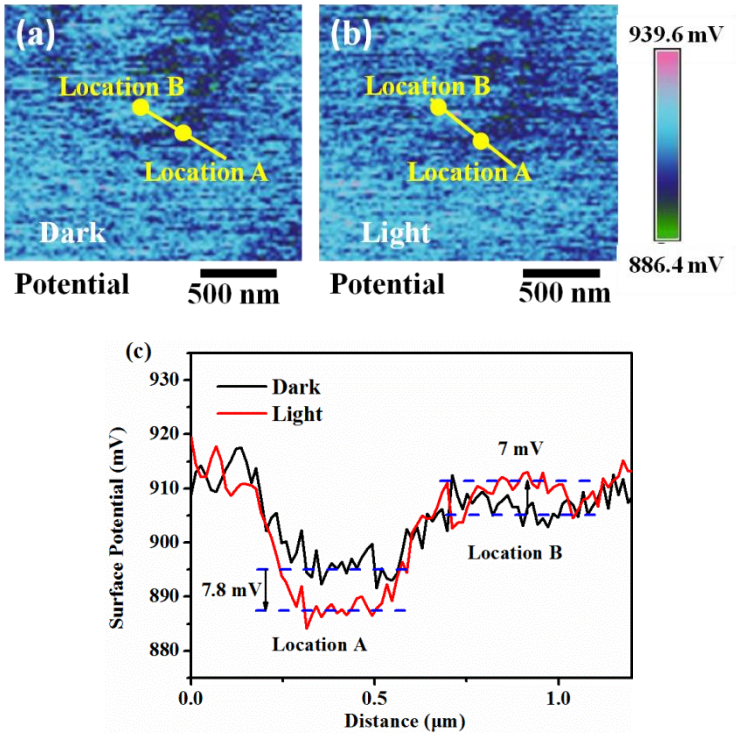


Fig. 9 Surface photovoltage distribution of CCN-20 in the dark (a) and visible light irradiation (b). (c) Surface photovoltage of CCN-20 under dark and visible light irradiation.

The surface potential of CCN-20 was measured by the KPFM measurements in the dark and λ > 400 nm conditions to ascertain the migration direction of photogenerated carriers during the reaction. The microscopic morphology of CCN-20 in virtue of KPFM (Fig. S9) was clearly observed that CN Ns (denoted as locationB) was partially surrounded by the $Cu_2O$ (denoted as location A). Figs. 9a and 9b show the surface photovoltage distribution of CCN-20 under dark and visible light irradiation conditions. Fig. 9c shows the corresponding surface potential from locations A to B. It can be seen that the surface potential decreased by approximately 7.8 mV at $Cu_2O$ and increased by approximately 7 mV at CN Ns after illumination. For comparison, the surface potential of pure CN Ns was measured. As shown in Fig. S10, the surface potential of pure CN Ns reduced slightly under visible light irradiation. The above results indicating that the photogenerated electrons migrated from CN Ns to

$Cu_2O$ under visible light irradiation. This means that an electric field ($E$) is established in the space charge region near the interface inside the composite material.

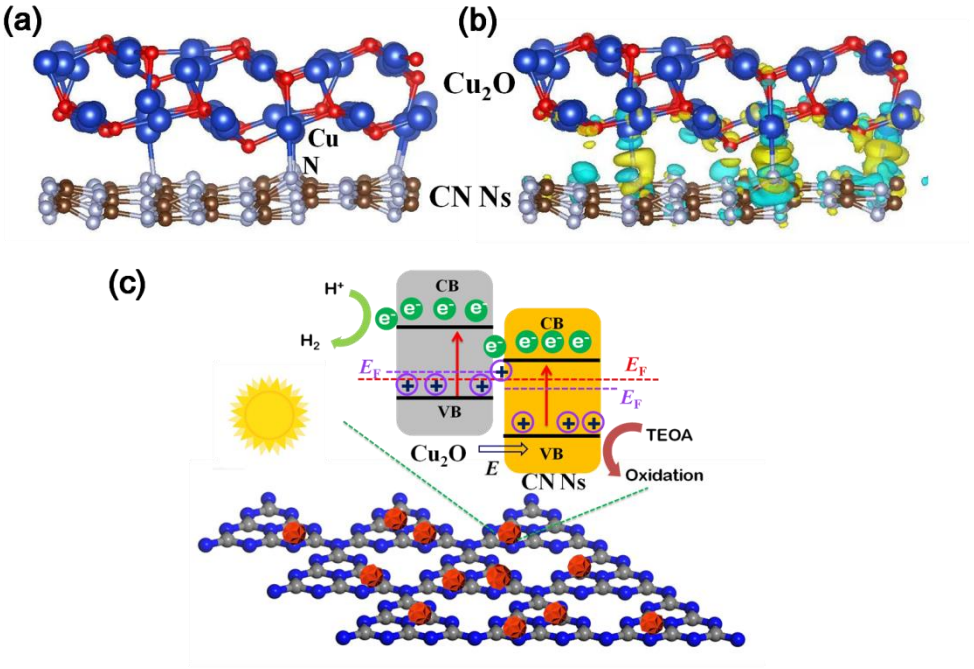


Fig. 10 (a) The optimized structure and (b) the side view of charge density difference of CCN-x. heterostructure. (c) Proposed mechanism for enhanced photocatalytic activities of CCN-x samples.

To further identify the interaction between $Cu_2O$ and CN Ns, the density functional theory (DFT) calculations were carried out. The optimized structure of CCN-x heterostructure is shown in Fig. 10a. The coordinative Cu atoms were from the (111) crystal plane of $Cu_2O$. Fig. 10b shows the side view of charge density difference of the composite, in which the yellow and blue iso-surfaces denote the accumulation and depletion of electron density, respectively. It can be noted that the electron cloud density shows distinctly localized distribution between Cu and N atoms. This result suggests that there are intense bonding effects between the Cu atoms in $Cu_2O$ and the N atoms in CN Ns, which is in accordance with the above FT-IR and XPS results.

Based on the energy band structures of CN Ns and $Cu_2O$ that have been evaluated above, the

Fermi level of electrons in $Cu_2O$ is higher than that in CN Ns. When $Cu_2O$ nanoparticles were grown on the surface of CN Ns, heterojunctions would form at the interface. Electrons would transfer from the Fermi level of $Cu_2O$ to that of CN Ns under the influence of the Fermi level difference until equilibrium was reached. As a consequence of the electron transport process, an inner electric field (*E*) point out from $Cu_2O$ into CN Ns can be formed in the space charge region near the interface (as presented in Fig. 10c).

When the CCN-x composite catalysts are irradiated by visible light, electrons can be excited from the VB to CB in both $Cu_2O$ and CN Ns. Driven by the electric field force, the electrons at the CB of CN Ns move to the interface and are trapped by the holes coming from the VB of $Cu_2O$. The removal of holes would reduce the photocorrosion of $Cu_2O$, increasing its stability. Meanwhile, photoinduced electrons at $Cu_2O$ CB migrate to the surface and participate in the $H_2$ production process. As a result, the heterojunction effectively separates photoinduced carriers. Furthermore, the electrons at the CB of $Cu_2O$ that have better redox capacity can be effectively used in the photocatalytic process. Briefly, the construction of $Cu_2O$/CN Ns "Z-scheme" heterojunction can effectively enhance the photocatalytic $H_2$ evolution efficiency.

## 4 Conclusions

In summary, $Cu_2O$ nanoparticles were grown on the surface of CN Ns to inhibit its photocorrosion. The experimental results confirmed that heterojunctions were produced in the CCN-x composite. The CCN-20 sample exhibited the maximum photocatalytic $H_2$ production rate (1796.8 μmol/g/h), which was about two times greater than that of bare CN Ns (about eight times higher than that of pure $Cu_2O$). Furthermore, the CCN-20 sample also exhibits an enhanced activity towards TC degradiation. The photoelectrochemical test confirmed the CCN-20 sample's high charge transfer and separation

efficiency, which is beneficial for increasing photocatalytic activity. At the same time, the “Z-scheme” photocatalysis mechanism is advantageous for increasing the redox capacity of the composite photocatalyst. This work provides a facile and feasible approach to construct new g-$C_3N_4$-based photocatalysts, which have great potential for application in the fields of new energy and environmental purification.

**Acknowledgment**

This work was supported by Hainan Provincial Natural Science Foundation of China (2019RC180).

**Declaration of interests**

The authors declare that they have no known competing financial interests or personal relationships that could have appeared to influence the work reported in this paper.

**Supplementary Material**

Please refer to Supporting Information for Experimental and Figures for supplementary instruction.

**References**

[1] S. Luo, X. Ren, H. Lin, H. Song, J. Ye, Plasmonic photothermal catalysis for solar-to-fuel conversion: current status and prospects, Chem. Sci. 12 (2021) 5701-5719.

[2] R. Yang, J. Liu, B. Wang, R. Wang, Y. Song, Y. Hua, C. Wang, Y. She, J. Yuan, H. Xu, H. Li, Synergistic effect of isolated Co and Fe dual active sites boosting the photocatalytic hydrogen evolution reaction, J Alloy. Compd. 895 (2022) 162290.

[3] J. Yu, J. Low, W. Xiao, P. Zhou, M. Jaroniec, Enhanced photocatalytic $CO_2$ reduction activity of anatase $TiO_2$ by coexposed {001} and {101} facets, J. Am. Chem. Soc. 136 (2014) 8839–8842.

[4]R. Yang, J. Liu, B. Wang, R. Wang, Y. Song, Y. Hua, C. Wang, Y. She, J. Yuan, H. Xu, Self-assembly and boosted photodegradation properties of perylene diimide via different solvents, New J. Chem. 45 (2021) 21701–21707.

[5] Y. Li, X. Wang, H. Huo, Z. Li, J. Shi, A novel binary visible-light-driven photocatalyst type-I $CdIn_2S_4$/g-$C_3N_4$ heterojunctions coupling with $H_2O_2$: Synthesis, characterization, photocatalytic activity for Reactive Blue 19 degradation and mechanism analysis, Colloid. Surface. A. (2019) 124322.

[6] S.H. Hsu, J. Miao, L. Zhang, J. Gao, H. Wang, H. Tao, S.F. Hung, A. Vasileff, S.Z. Qiao, B. Liu, An Earth-Abundant Catalyst-Based Seawater Photoelectrolysis System with 17.9% Solar-to-Hydrogen Efficiency, Adv. Mater. 30 (2018) 1707261.

[7] Y. Li, J. Feng, H. Li, X. Wei, R. Wang, A. Zhou, Photoelectrochemical splitting of natural seawater with α-$Fe_2O_3$/$WO_3$ nanorod arrays, Int. J. Hydrogen. Energ. 41 (2016) 4096-4105.

[8] Q. Zhang, Y. M. Li, J. B. Zhong, J. Z. Li, Facile construction of CuO/g-$C_3N_4$ heterojunctions with promoted photocatalytic hydrogen generation behaviors, Fuel. 353 (2023)129224.

[9] T. Takata, J. Jiang, Y. Sakata, M. Nakabayashi, N. Shibata, V. Nandal, K. Seki, T. Hisatomi, K. Domen, Photocatalytic water splitting with a quantum efficiency of almost unity, Nature 581 (2020) 411-414.

[10] S. Cao, L. Piao, Considerations for a More Accurate Evaluation Method for Photocatalytic Water Splitting, Angew. Chem. Int. Edit. 59 (2020) 18312-18320.

[11] H. Liu, Z. Jin, Z. Xu, Z. Zhang, D. Ao, Fabrication of $ZnIn_2S_4$–g-$C_3N_4$ sheet-on-sheet nanocomposites for efficient visible-light photocatalytic $H_2$ evolution and degradation of organic

pollutants, RSC Adv. 5 (2015) 97951-97961.

[12] R. Chen, S. Pang, H. An, J. Zhu, S. Ye, Y. Gao, F. Fan, C. Li, Charge separation via asymmetric illumination in photocatalytic $Cu_2O$ particles, Nat. Energy 3 (2018) 655-663.

[13] A. Paracchino, V. Laporte, K. Sivula, M. Grätzel, E. Thimsen, Highly active oxide photocathode for photoelectrochemical water reduction, Nat. Mater. 10 (2011) 456-461.

[14] L. Pan, J.H. Kim, M.T. Mayer, M.K. Son, A. Ummadisingu, J.S. Lee, A. Hagfeldt, J. Luo, M. Grätzel, Boosting the performance of $Cu_2O$ photocathodes for unassisted solar water splitting devices, Nat. Catal.1 (2018) 412-420.

[15] C.Y. Toe, Z. Zheng, H. Wu, J. Scott, R. Amal, Y.H. Ng, Photocorrosion of Cuprous Oxide in Hydrogen Production: Rationalising Self-Oxidation or Self-Reduction, Angew. Chem. Int. Edit. 57 (2018) 13613-13617.

[16] L. Xiong, H. Xiao, S. Chen, Z. Chen, X. Yi, S. Wen, G. Zheng, Y. Ding, H. Yu, Fast and simplified synthesis of cuprous oxide nanoparticles: annealing studies and photocatalytic activity, RSC Adv. 4 (2014) 62115-62122.

[17] Y. H. Zhang, M. M. Liu, J. L. Chen, S. M. Fang, P. P. Zhou, Recent advances in $Cu_2O$-based composites for photocatalysis: a review, Dalton Trans. 50 (2021) 4091.

[18] T. Wei, Y.N. Zhu, X. An, L.M. Liu, X. Cao, H. Liu, J. Qu, Defect Modulation of Z-Scheme $TiO_2/Cu_2O$ Photocatalysts for Durable Water Splitting, ACS Catal. 9 (2019) 8346-8354.

[19] J. Xu, Z. Z. Li, Z. L. Liu, S. M. Xu, X. Y. Liu, Zn-MOF loading $Cu_2O$ cube to construct hierarchical solid cage to improve photocatalytic hydrogen evolution, J. Ind. Eng. Chem. 126 (2023) 557-567.

[20] L. Fan, J. Han, K. Wei, C. Ma, S. Feng, Y. Zhou, X. Dai, Z. W. Ye, Y. Wang, Mn-doped CdS/$Cu_2O$:

511 An S-scheme heterojunction for photocatalytic hydrogen production, J. Alloy Compd. 960 (2023)
512 170382.
513 [21] Q. Zhu, Y. Wang, F. Chen, X. H. Yang, H. Ou, S. X. Xiong, H. T. Fu, Enhanced photocatalytic $H_2$
514 production performance of Au@$Cu_2O$-$Ta_3N_5$ discrete ternary core-shell spheres, Appl. Surf. Sci. 635
515 (2023) 157682.
516 [22] Y. C. Chang, S. Y. Syu, M. Y. Lu, Fabrication of $In(OH)_3$–$In_2S_3$–$Cu_2O$ nanofiber for highly
517 efficient photocatalytic hydrogen evolution under blue light LED excitation, Int. J. Hydrogen Energ.
518 48 (2023) 9318-9332.
519 [23] J. Zhang, H. Ma, Z. Liu, Highly efficient photocatalyst based on all oxides $WO_3$/$Cu_2O$
520 heterojunction for photoelectrochemical water splitting, Appl. Catal. B: Environ. 201 (2017) 84-91.
521 [24] B. J. Ng, J. Y. Tang, L. Y. Ow, X. Y. Kong, Y. H. Ng, L. K. Putri, S. P. Chai, Nanoscale pen
522 junction integration via the synergetic hybridization of facet-controlled $Cu_2O$ and defect-modulated
523 g-$C_3N_4$-x atomic layers for enhanced photocatalytic water splitting, Mater. Today Energy 29 (2022)
524 101102.
525 [25] F.Y. Tian, X. Y. Wu, S. Liu, Y. W. Gu, Z. Z. Lin, H. L. Zhang, X. M. Yan, G. F. Liao, Boosting
526 photocatalytic $H_2$ evolution through interfacial manipulation on a lotus seedpod shaped $Cu_2O$/g-$C_3N_4$
527 p-n heterojunction, Sustain. Energy Fuels 7 (2023) 786-796.
528 [26] J. Chen, S. H. Shen, P. H. Guo, M. Wang, P. Wu, X. Wang, L. J. Guo, In-situ reduction synthesis of
529 nano-sized $Cu_2O$ particles modifying g-$C_3N_4$ for enhanced photocatalytic hydrogen production, Appl.
530 Catal. B: Environ. 152-153 (2014) 335-341.
531 [27] Z. Zhao, Y. Sun, F. Dong, Graphitic carbon nitride based nanocomposites: a review, Nanoscale 7
532 (2015) 15-37.

[28] G. Liao, Y. Gong, L. Zhang, H. Gao, G.J. Yang, B. Fang, Semiconductor polymeric graphitic carbon nitride photocatalysts: the “holy grail” for the photocatalytic hydrogen evolution reaction under visible light, Energ. Environ. Sci. 12 (2019) 2080-2147.

[29] J. Liu, Q. Jia, J. Long, X. Wang, Z. Gao, Q. Gu, Amorphous NiO as co-catalyst for enhanced visible-light-driven hydrogen generation over g-$C_3N_4$ photocatalyst, Appl. Catal., B: Environ. 222 (2018) 35-43.

[30] W.J. Wang, G.Y. Li, T.C. An, D.K.L. Chan, J.C. Yu, P.K. Wong, Photocatalytic hydrogen evolution and bacterial inactivation utilizing sonochemical-synthesized g-$C_3N_4$/red phosphorus hybrid nanosheets as a wide-spectral-responsive photocatalyst: The role of type I band alignment, Appl. Catal. B: Environ. 238 (2018) 126-135.

[31] B. L. Dai, Y. Y. Li, J.M. Xu, C. Sun, S.J. Li, W. Zhao, Photocatalytic oxidation of tetracycline, reduction of hexavalent chromium and hydrogen evolution by $Cu_2O$/g-$C_3N_4$ S-scheme photocatalyst: Performance and mechanism insight, Appl. Surf. Sci. 592 (2022) 153309.

[32] M. Ou, S. Wan, Q. Zhong, S. Zhang, Y. Song, L. Guo, W. Cai, Y. Xu, Hierarchical Z-scheme photocatalyst of g-$C_3N_4$@Ag/$BiVO_4$ (040) with enhanced visible-light-induced photocatalytic oxidation performance, Appl. Catal. B: Environ. 221 (2018) 97-107.

[33] B. G. Xu, B. Wang, H. Y. Zhang, P. Yang, Z-Scheme $Cu_2O$ Nanoparticle/Graphite Carbon Nitride Nanosheet Heterojunctions for Photocatalytic Hydrogen Evolution, ACS Appl. Nano Mater. 5 (2022) 8475-8483.

[34] S. Zhang, Y. Zhao, R. Shi, C. Zhou, G.I.N. Waterhouse, Z. Wang, Y. Weng, T. Zhang, Sub-3 nm Ultrafine $Cu_2O$ for Visible Light Driven Nitrogen Fixation, Angew. Chem. Int. Edit 60 (2020) 2554-2560.

555 [35] J. Liang, X. Yang, Y. Wang, P. He, H. Fu, Y. Zhao, Q. Zou, X. An, A review on g-$C_3N_4$
556 incorporated with organics for enhanced photocatalytic water splitting, J. Mater. Chem. A 9 (2021)
557 12898-12922.
558 [36] P. Niu, L. Zhang, G. Liu, H.M. Cheng, Graphene-Like Carbon Nitride Nanosheets for Improved
559 Photocatalytic Activities, Adv. Funct. Mater. 22 (2012) 4763-4770.
560 [37] Y. Cao, Z. Xing, Z. Li, X. Wu, M. Hu, X. Yan, Q. Zhu, S. Yang, W. Zhou, Mesoporous black
561 $TiO_{2-x}$/Ag nanospheres coupled with g-$C_3N_4$ nanosheets as 3D/2D ternary heterojunctions visible light
562 photocatalysts, J. Hazard. Mater. 343 (2018) 181-190.
563 [38] A. Kumar, A. Kumar, G. Sharma, A.a.H. Al-Muhtaseb, M. Naushad, A.A. Ghfar, F.J. Stadler,
564 Quaternary magnetic BiOCl/g-$C_3N_4$/$Cu_2O$/$Fe_3O_4$ nano-junction for visible light and solar powered
565 degradation of sulfamethoxazole from aqueous environment, Chem. Eng. J. 334 (2018) 462-478.
566 [39] J. Hafner, Ab-Initio simulations of materials using VASP: Density-Functional theory and beyond, J.
567 Comput. Chem. 29 (2008) 2044-2078.
568 [40] P. E. Blöchl, Projector augmented-wave method, Phys. Rev. B 50 (1994) 17953.
569 [41] J. P. Perdew, K. Burke, M. Ernzerhof, Generalized gradient approximation made simple, Phys. Rev.
570 Lett. 77(1996) 3865.
571 [42] S. Grimme, Semiempirical GGA-Type density functional constructed with a Long-Range
572 dispersion correction, J. Comput. Chem. 27 (2006) 1787.
573 [43] Y. Z. Zhang, W. Zhou, L. X. Jia, X. Tan, Y. L. Chen, Q. Huang, B. Y. Shao, T. Yu, Visible light
574 driven hydrogen evolution using external and confined CdS:Effect of chitosan on carriers separation,
575 Appl. Catal. B Environ. 277 (2020) 119152.
576 [44] W. Q. Cui, W. J. An, L. Liu, J. S. Hu, Y. H. Liang, Novel $Cu_2O$ quantum dots coupled flower-like

577 BiOBr for enhanced photocatalytic degradation of organic contaminant, J. Hazard. Mater. 280 (2014)
578 417-427.
579 [45] X. Wang, K. Maeda, A. Thomas, K. Takanabe, G. Xin, J.M. Carlsson, K. Domen, M. Antonietti, A
580 metal-free polymeric photocatalyst for hydrogen production from water under visible light, Nat. Mater.
581 8 (2009) 76-80.
582 [46] D. Tran, H. Vuong, D. Nguyen, P. Ly, P. Phan, V. Khoi, P. Mai, N. Hieu, Revisiting the roles of
583 dopants in g-$C_3N_4$ nanostructures for piezo-photocatalytic production of $H_2O_2$: a case study of selenium
584 and sulfur, Nanoscale Adv. 5 (2023) 2327.
585 [47] U. Rajaji, S.V. Selvi, S.M. Chen, S. Chinnapaiyan, T.W. Chen, M. Govindasamy, A nanocomposite
586 consisting of cuprous oxide supported on graphitic carbon nitride nanosheets for non-enzymatic
587 electrochemical sensing of 8-hydroxy-2′-deoxyguanosine, Microchim. Acta 187 (2020) 459.
588 [48] J. Ma, X. Tan, T. Yu, X. Li, Fabrication of g-$C_3N_4$/$TiO_2$ hierarchical spheres with reactive {001}
589 $TiO_2$ crystal facets and its visible-light photocatalytic activity, Int. J. Hydrogen Energ. 41 (2016)
590 3877-3887.
591 [49] Y. Pu, H.Y. Chou, W.S. Kuo, K. H. Wei, Y.J. Hsu, Interfacial charge carrier dynamics of cuprous
592 oxide-reduced graphene oxide ($Cu_2O$-rGO) nanoheterostructures and their related visible-light-driven
593 photocatalysis, Appl. Catal. B Environ. 204 (2017) 21-32.
594 [50] Z. Y. Yao, T. Gu, T. L. Lu, Y. Z. Zhan, Solvothermally synthesized spherical copper
595 hydroxyfluoride (CuOHF) as an efficient heterogeneous Fenton catalyst for degrading organic
596 pollutants, Desalin. Water Treat. 204 (2020) 400-412.
597 [51] B. Wu, L. Zhang, B. Jiang, Q. Li, C. Tian, Y. Xie, W. Li, H. Fu, Ultrathin Porous Carbon Nitride
598 Bundles with an Adjustable Energy Band Structure toward Simultaneous Solar Photocatalytic Water

599 Splitting and Selective Phenylcarbinol Oxidation, Angew. Chem. Int. Edit 60 (2021) 4815-4822.

600 [52] P. P. Ly, D. Nguyen, T. Luu, N. Hung, P. T. Hue, N. T. N. Hue, M. T. Pham, T. D. T. Ung, D. D.

601 Bich, P. D. M. Phan, N. H. Anh, H. P. Toan, D. Bui, V. Dao, S. H. Hur, H. Vuong, Insights into molten

602 salts induced structural defects in graphitic carbon nitrides for piezo-photocatalysis with multiple $H_2O_2$

603 production channels, Adv. Sustainable. Syst. (2023) 2300470.

604 [53] C. Zhou, S. Wang, Z. Zhao, Z. Shi, S. Yan, Z. Zou, A facet-dependent schottky-junction electron

605 shuttle in a $BiVO_4${010}-Au-$Cu_2O$ Z-scheme photocatalyst for efficient charge separation, Adv. Funct.

606 Mater. 28(31) (2018) 1801214.

607 [54] J. X. Bai, W. L. Chen, L. Hao, R. C. Shen, P. Zhang, N. Li, X. Li, Assembling $Ti_3C_2$ MXene into

608 $ZnIn_2S_4$-$NiSe_2$ S-scheme heterojunction with multiple charge transfer channels for accelerated

609 photocatalytic $H_2$ generation, Chem. Eng. J. 447 (2022) 137488.

610 [55] M. E. Malefane, P. J. Mafa, T. T. I. Nkambule, M. E. Managa, A. T. Kuvarega, Modulation of

611 Z-scheme photocatalysts for pharmaceuticals remediation and pathogen inactivation: Design Devotion,

612 Concept Examination, and Developments, Chem. Eng. J. 452 (2022) 138894.

613 [56] W. Jo, T. S. Natarajan, Influence of $TiO_2$ morphology on the photocatalytic efficiency of direct

614 Z-scheme g-$C_3N_4$/$TiO_2$ photocatalysts for isoniazid degradation, Chem. Eng. J. 281 (2015) 549-565.

615 [57] P. D. M. Phan, D. Nguyen, N. H. Anh, H. P. Toan, P. P. Ly, D. P. Bui, S. H. Hur, T. D. T. Ung, D. D.

616 Bich, H. T. Vuong, S‐Scheme heterostructured CdS/g-$C_3N_4$ nanocatalysts for Piezo-photocatalytic

617 synthesis of $H_2O_2$, ACS Appl. Nano Mater. 6 (2023) 16702-16715.

618 [58] R. Chen, J. Yu, W. Xiao, Hierarchically porous $MnO_2$ microspheres with enhanced adsorption

619 performance, J. Mater. Chem. A. 1(2013) 11682–11690.

620 [59] K. Q. Lu, Y. Chen, X. Xin, Y. J. Xu, Rational utilization of highly conductive, commercial Elicarb

graphene to advance the graphene-semiconductor composite photocatalysis, Appl. Catal. B Environ. 224 (2018) 424-432.

[60] Y. Li, S. Ouyang, H. Xu, W. Hou, M. Zhao, H. Chen, J. Ye, Targeted Exfoliation and Reassembly of Polymeric Carbon Nitride for Efficient Photocatalysis, Adv. Funct. Mater. (2019) 1901024.

[61] J. H. Yang, D. Wang, H. X. Han, C. Li, Roles of cocatalysts in photocatalysis and photoelectrocatalysis, Acc. Chem. Res. 46 (2013) 1900-1909.

[62] J. Ma, C. Liang, C. Yu, H. Li, H. Xu, Y. J. Hua, C.T. Wang, BiOBr microspheres anchored with $Cu_2O$ nanoparticles and rGO: A Z-scheme heterojunction photocatalyst for efficient reduction of Cr(VI) under visible light irradiation, Appl. Surf. Sci. 609 (2023) 155247.

[63] J. Ma, C. Liang, H. Li, H. Xu, Y.J. Hua, C.T. Wang, A novel composite material based on hydroxylated g-$C_3N_4$ and oxygen-vacant $TiO_2$ for improvement of photocatalytic performance, Appl. Surf. Sci. 546 (2021) 149085.

[64] S. Guo, Z. Deng, M. Li, B. Jiang, C. Tian, Q. Pan, H. Fu, Phosphorus-Doped Carbon Nitride Tubes with a Layered Micro-nanostructure for Enhanced Visible-Light Photocatalytic Hydrogen Evolution, Angew. Chem. Int. Edit. 55 (2016) 1830-1834.